

# An experimental and simulation study on build thickness dependent microstructure for electron beam melted Ti-6Al-4V

Tan, Xipeng; Kok, Yihong; Tan, Yu Jun; Vastola, Guglielmo; Pei, Qing Xiang; Zhang, Gang; Zhang, Yong-Wei; Tor, Shu Beng; Leong, Kah Fai; Chua, Chee Kai

2015

Tan, X., Kok, Y., Tan, Y. J., Vastola, G., Pei, Q. X., Zhang, G., et al. (2015). An experimental and simulation study on build thickness dependent microstructure for electron beam melted Ti-6Al-4V. *Journal of alloys and compounds*, 646, 303-309.

<https://hdl.handle.net/10356/79369>

<https://doi.org/10.1016/j.jallcom.2015.05.178>

---

© 2015 Elsevier B.V. This is the author created version of a work that has been peer reviewed and accepted for publication by *Journal of alloys and compounds*, Elsevier B.V. It incorporates referee's comments but changes resulting from the publishing process, such as copyediting, structural formatting, may not be reflected in this document. The published version is available at: [<http://dx.doi.org/10.1016/j.jallcom.2015.05.178>].

*Downloaded on 03 Apr 2024 11:15:41 SGT*

# Accepted Manuscript

An experimental and simulation study on building thickness dependent microstructure for electron beam melted Ti-6Al-4V

Xipeng Tan, Yihong Kok, Yu Jun Tan, Guglielmo Vastola, Qing Xiang Pei, Gang Zhang, Yong-Wei Zhang, Shu Beng Tor, Kah Fai Leong, Chee Kai Chua



PII: S0925-8388(15)30078-5

DOI: [10.1016/j.jallcom.2015.05.178](https://doi.org/10.1016/j.jallcom.2015.05.178)

Reference: JALCOM 34300

To appear in: *Journal of Alloys and Compounds*

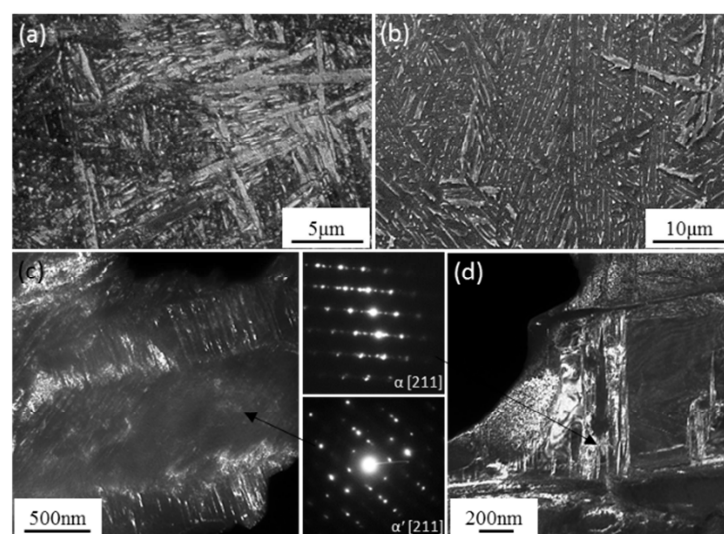
Received Date: 7 May 2015

Revised Date: 27 May 2015

Accepted Date: 28 May 2015

Please cite this article as: X. Tan, Y. Kok, Y.J. Tan, G. Vastola, Q.X. Pei, G. Zhang, Y.-W. Zhang, S.B. Tor, K.F. Leong, C.K. Chua, An experimental and simulation study on building thickness dependent microstructure for electron beam melted Ti-6Al-4V, *Journal of Alloys and Compounds* (2015), doi: 10.1016/j.jallcom.2015.05.178.

This is a PDF file of an unedited manuscript that has been accepted for publication. As a service to our customers we are providing this early version of the manuscript. The manuscript will undergo copyediting, typesetting, and review of the resulting proof before it is published in its final form. Please note that during the production process errors may be discovered which could affect the content, and all legal disclaimers that apply to the journal pertain.



## An experimental and simulation study on building thickness dependent microstructure for electron beam melted Ti-6Al-4V

Xipeng Tan <sup>1,\*</sup>, Yihong Kok <sup>1</sup>, Yu Jun Tan <sup>1</sup>, Guglielmo Vastola <sup>2,\*</sup>, Qing Xiang Pei <sup>2</sup>, Gang Zhang <sup>2</sup>,  
Yong-Wei Zhang <sup>2</sup>, Shu Beng Tor <sup>1</sup>, Kah Fai Leong <sup>1</sup>, Chee Kai Chua <sup>1</sup>

<sup>1</sup> Singapore Centre for 3D Printing, School of Mechanical & Aerospace Engineering, Nanyang Technological University, HW1-01-05, 2A Nanyang Link, Singapore 637372

<sup>2</sup> Institute of High Performance Computing, A\*Star, 1 Fusionopolis Way, #16-16 Connexis, Singapore 138632

\*Corresponding authors. E-mail: [xptan@gmail.com](mailto:xptan@gmail.com) & [vastolag@ihpc.a-star.edu.sg](mailto:vastolag@ihpc.a-star.edu.sg)

### Abstract

Build thickness dependent microstructure of electron beam melted (EBM<sup>®</sup>) Ti-6Al-4V has been investigated from both experiment and simulation using four block samples with thicknesses of 1, 5, 10 and 20 mm. We observe a mixed microstructure of alternate  $\alpha/\beta$  with some  $\alpha'$  martensite inside the 1 mm-thick sample. By contrast, only the alternate  $\alpha/\beta$  microstructure with both colony and basket-weave morphologies occurs inside the 5 mm-, 10 mm- and 20 mm-thick samples. It is found that  $\beta$  spacing is constantly increased with the build thickness, leading to an obvious decrease in microhardness. Finite element method (FEM) simulations show that cooling rates and thermal profiles during EBM process are favorable for the formation of martensite. Moreover, full-scale FEM simulations reveal that the average temperature inside the samples is higher as the build thickness increases. It suggests that martensitic decomposition is faster in thicker samples, which is in good agreement with the experimental observations.

**Keywords:** Additive manufacturing; Electron beam melting; Titanium alloys; Martensitic transformations; Finite element simulations

### 1. Introduction

Electron beam melting (EBM<sup>®</sup>) is an additive manufacturing (commonly known as 3D printing) technique using a focused electron beam to selectively melt a metallic powder bed under high vacuum,

directed by a computer aided design (CAD) model. EBM is capable of producing functional parts with good mechanical properties rapidly and energy-efficiently [1]. Moreover, EBM-built part has low residual stress because an elevated build temperature is involved [2]. Therefore, post-processing heat treatment may not be necessary for EBM-built functional parts.

Ti-6Al-4V is the most widely used titanium alloy. Due to its high strength-to-weight ratio, outstanding corrosion resistance and good biocompatibility, Ti-6Al-4V has shown a great application potential in aerospace, marine & offshore, medical devices, etc. [3]. EBM is a preferred AM technique for fabricating Ti-6Al-4V parts because of titanium's high affinity for oxygen. EBM-built Ti-6Al-4V parts were most investigated till date [4]. It is known that columnar prior  $\beta$  grains would form in EBM-built Ti-6Al-4V, which is attributed to the high thermal gradient of the EBM process [5][6]. Safdar et al. found that a transformed  $\alpha/\beta$  microstructure consisting of Widmanstätten  $\alpha$  platelets and rod-like  $\beta$  phase was formed within the columnar prior  $\beta$  grains [6]. Much finer grains were found in EBM-built Ti-6Al-4V compared to casting Ti-6Al-4V, owing to its very rapid cooling [7]. In general, the tensile properties of EBM-built Ti-6Al-4V parts are comparable with that of wrought form and better than that of cast form [8]. However, knowledge and prediction of the exact amount of the different phases in the final EBM-built part still encounter many open questions, including whether martensite will form or not during EBM process [9]. For example, recent investigations have clearly shown the formation of martensite in selective laser melting (SLM)-built Ti-6Al-4V samples [10] due to the higher cooling rates experienced in the SLM process compared to EBM. Because the amount of martensite has a direct impact on the mechanical properties, including strength and fatigue resistance [11], the study on microstructural evolution involved in EBM process is imperative.

In this paper, we investigate the microstructural variation of EBM-built Ti-6Al-4V parts with different thicknesses using both experiments and modeling methods. In particular, we experimentally demonstrate the formation and decomposition of  $\alpha'$  martensite inside EBM-built Ti-6Al-4V samples with different thicknesses, and perform finite element method (FEM) simulations to further prove the possibility of martensitic formation and decomposition in the samples with different thickness. Our combined experimental and modeling approach provides further insight to understand the formation and evolution of microstructure during EBM of Ti-6Al-4V, and suggests a route towards the control of martensite phase in as-built EBM parts.

## 2. Experimental

All samples for evaluation were built using an Arcam A2XX (Arcam AB, Sweden) EBM machine (Fig. 1a). Ti-6Al-4V ELI (Grade 23) powder supplied by Arcam AB was used. The powder size distribution ranges from 45 to 100  $\mu\text{m}$  (Fig. 1b and c). The nominal composition of as-supplied powders

is 6.0Al-4.0V-0.03C-0.1Fe-0.1O-0.01N-<0003H and Ti Bal. (in wt.%). Recycling of non-melted and/or sintered powder was achieved via the powder recovery system (PRS) and a vibrating sieve (mesh size  $\leq 150 \mu\text{m}$ ). In order to investigate the thickness dependent microstructure of EBM-built parts, three types of block samples with varying thicknesses of 1 mm, 5 mm, 10 mm and 20 mm ( $100 \text{ mm} \times 1 \text{ mm} \times 30 \text{ mm}$ ,  $100 \text{ mm} \times 5 \text{ mm} \times 30 \text{ mm}$ ,  $100 \text{ mm} \times 10 \text{ mm} \times 30 \text{ mm}$  and  $100 \text{ mm} \times 20 \text{ mm} \times 30 \text{ mm}$ ) were fabricated as shown in Fig. 1d. They were termed 1mm, 5mm, 10mm and 20mm samples, respectively. They were built directly onto the preheated start plate by selectively melting layers of  $50 \mu\text{m}$  under a controlled vacuum in the temperature range of 600-650 °C. The entire building process was kept under vacuum at  $\sim 2\text{e-}3 \text{ mBar}$ , controlled by using high-purity helium as regulating gas in order to prevent powder charging.

X-ray diffraction (XRD; PANalytical Empyrean; Cu K $\alpha$ ; step size of 0.01°), scanning electron microscopy (SEM; JEOL JMS-6700F; 20 kV) and transmission electron microscopy (TEM; JEOL-2010; 200 kV) were used to examine the microstructure of as-built Ti-6Al-4V. SEM samples were etched in Kroll's reagent (1-3% HF, 2-6% HNO<sub>3</sub>, and 91-97% H<sub>2</sub>O) for 10 seconds. Quantitative image analysis was carried out by using Image J software. Thin sample sections were ground to  $\sim 100 \mu\text{m}$  and then manually ground to  $\sim 50 \mu\text{m}$  with silicon carbide paper under the protection of water. Standard 3 mm (in diameter) TEM discs were punched out from the  $50 \mu\text{m}$  thick sections. The disc was then dimpled on both sides and then Ion milled within 4-8 °. Ion milling voltage varied from 3.5 to 4.5 V. Phase identification was carried out by means of XRD and selected area electron diffraction (SAED). Vickers microhardness tests were carried out on the metallography samples using a Future Tech FM-300e micro hardness tester. A load of 1 kg and a 15 seconds dwell time were adopted.

### 3. Simulation models

FEM simulations were performed to study the thermal history of the parts during EBM process. Because a simulation of the real-size samples would be impractical, requiring too many mesh elements, a choice was made to simulate either the beam scanning and absorption with high accuracy, focusing on a small region of the samples, or the overall thermal evolution of the entire samples, while reducing the modeling accuracy of the beam. This was accomplished by designing two separate simulation models. In the first model, focus was given to a small region of the sample, where the beam intensity profile and beam absorption was carefully taken into account to reproduce the cooling rates and thermal gradients typical of EBM [12]. In the second model, the beam was taken into account in an effective way, allowing for a simulation of the entire sample size. Thus it enables us study the temperature evolution through the real scale samples.

For the first model, a two-dimensional mesh with a dimension of  $2.5 \text{ mm} \times 500 \text{ }\mu\text{m}$  was built with quadrilateral elements with an element size of  $25 \text{ }\mu\text{m} \times 25 \text{ }\mu\text{m}$ . The electron beam was modeled as a moving Gaussian heat source [13], where the peculiar absorption profile of an electron beam was considered [12]. Beam absorption depth was set to be  $28 \text{ }\mu\text{m}$  [13], beam voltage 60 kV, beam current 10 mA, and spot size  $200 \text{ }\mu\text{m}$ , according to the working parameters of Arcam EBM machine [4]. Heat loss was considered from the top surface in terms of radiation, where the emissivity of Ti-6Al-4V was set to be 0.35 [14]. No heat convection was included because the process occurs in vacuum. The other boundaries of the mesh were kept at a fixed temperature of  $650 \text{ }^{\circ}\text{C}$ . The initial temperature was also set to be  $650 \text{ }^{\circ}\text{C}$  to reproduce the pre-heating step that precedes in actual EBM building. The change in different phases (powder, melt, solid) during melting and solidification was considered following the approach developed earlier [15], where the thermal properties were dependent on the phase and they were taken from [16]. During the simulation, temperature distributions in the model were generated and temperature-time curves at selected locations were recorded. Fig. 2a and b show typical temperature profiles as the beam travelled from right to left. It is worth noting that Multispot contours were employed in the A2XX EBM machine. Due to the small mesh dimensions used for the first model, the so-called “dummy sweep” with a speed of 140 m/s will be used for small contour lengths that would be suitable for our model.

For the second model, calculations were designed in three-dimensions by reproducing the real dimensions of samples and embedding them into powder material, as shown in Fig. 3. Here, since the samples were simulated in real scale, the precise modeling of the beam becomes computationally intractable because it would require too many mesh elements. Therefore, it is necessary to model the EBM process in an equivalent way. As the scanning speed of electron beam is  $\sim 4.5 \text{ m/s}$ , the in-fill hatching takes seconds to complete the scan of one layer. Therefore, scanning along the direction perpendicular to in-fill hatching can be assumed to be instantaneous compared to that along the hatching direction. Using a scanning speed of  $4.5 \text{ m/s}$ , the effective beam speed along the hatching direction was estimated as  $14 \text{ mm/s}$ ,  $7 \text{ mm/s}$  and  $3.5 \text{ mm/s}$  for the 5mm, 10mm and 20mm samples, respectively. This estimate was computed considering that the build time for each sample is directly proportional to its cross-section area, and that the total build time was  $\sim 50$  seconds per layer. In this way, scan times of 7.1, 14.3, and 28.6 seconds were obtained for the 5mm, 10mm, and 20 mm samples respectively, while it was only 1.5 ms for the 1mm sample because of its fast scanning speed. For example, the effective beam heat profile is shown in Fig. 3c and d for the 20mm sample during scanning and cooling, respectively, where the beam size was taken of the order of the melt pool ( $2 \text{ mm}$ ) and the intensity was tuned such that the surface temperature was  $\sim 2400 \text{ }^{\circ}\text{C}$  [14]. Special attention was devoted to the simulation of the 1mm sample (Fig. 3a and b), because it consisted of pure contour melt scan. For this case, the beam speed was

set to be 140 m/s and beam scan was simulated in two passes, with an effective beam size of 4 mm, which is comparable to the length of the melt pool. In each of the four cases, a cooling step was modeled after the scan, where the cooling time was set to reproduce the actual time that the beam spends to scan the other samples. For example, the cooling time of the 20mm sample was equal to  $(7.1 + 14.3)$  seconds, i.e., the time that the beam took to scan the 5mm and 10mm samples, where the scan time for the 1mm sample was neglected because it is very short compared to the scan time of the other samples. The detailed list of effective scan speed, scan time, and cooling times is listed in Table 1 for each sample. In each simulation, the bulk material was embedded into a sufficient volume of powder material (Fig. 3e and f), where the powder was set with its relevant values for thermal conductivity and specific heat, and the cooling temperature was set at the mesh boundaries.

#### 4. Results and discussion

As-built EBM parts are not fully dense and void-free currently. A huge number of near-spherical pores (most of them falls into the size range of  $\sim 1\text{-}6\ \mu\text{m}$ ) as well as some lack-of-fusion defects were observed throughout the build. As the 1mm sample was built only by contour melting with a very fast beam scanning speed, it contains a higher porosity compared to other samples. Fig. 4 shows the XRD patterns for the 1mm and 10mm samples. It can be seen from Fig. 4a that the XRD peak positions are basically consistent for the two samples. The major peaks arise from  $\alpha$  phase and a small peak belongs to  $\beta$  (110) in the 10mm sample. An obvious peak broadening phenomenon could be observed in the 1mm sample in comparison with the 10mm sample (Fig. 4b), which suggests that a mixture of  $\alpha/\alpha'$  was formed inside the 1mm sample [17]. Fig. 5a reveals a mixed microstructure of alternate  $\alpha/\beta$  with acicular  $\alpha'$  martensite. The heavily twinned  $\alpha'$  could be identified as shown in Fig. 5c. By contrast, a typical alternate  $\alpha/\beta$  duplex microstructure with both colony and basket-weave morphology inside the 5mm sample was shown in Fig. 5b. Moreover, many microtwins exist inside  $\alpha$  phase (as revealed in Fig. 5d).

The phase evolution involved in the EBM processing of Ti-6Al-4V could be simplified as follows: As the electron beam scanned over the Ti-6Al-4V powder, melt pool formed and then was rapidly solidified into  $\beta$  grains. The prior  $\beta$  grains underwent a rapid cooling transforming into martensitic  $\alpha'$  phase. As additional layers were deposited, a near-isothermal annealing process at the build temperature of  $\sim 600\text{-}650\ ^\circ\text{C}$  enables the  $\alpha'$  martensite decompose into  $\alpha_{\text{Colony\&Basket-weave}}$  and  $\beta_{\text{Rod}}$ , followed by slowly cooling down to room temperature once the part was completed. Here, the cooling rates during solidification and cooling in solid were calculated to be in the range  $\sim 10^3\text{-}10^5\ \text{K s}^{-1}$  [5]. A martensite start temperature ( $M_s$ ) of  $800\ ^\circ\text{C}$  [3] and a critical cooling rate of  $>410\ ^\circ\text{C s}^{-1}$  [18] were accepted to be the two necessary requirements for the formation of  $\alpha'$  martensite. During the EBM process, it is known that the build temperature was below  $800\ ^\circ\text{C}$  and the cooling rate must be higher than  $410\ ^\circ\text{C s}^{-1}$  [5]. Thus,  $\alpha'$



martensite should be formed after melting. The observation of some retained  $\alpha'$  martensite inside 1mm sample also prove the aforementioned process.

Like other martensitic transformation,  $\alpha'$  will undergo a reversible reaction on cooling and heating, *i.e.*  $\beta \leftrightarrow \alpha'$ . In addition,  $\alpha'$  martensite will decompose into  $\alpha$  and  $\beta$  phases, *i.e.*  $\alpha' \rightarrow \alpha + \beta$ , when it is subjected to an isothermal annealing in the  $\alpha + \beta$  two phase field. It was proposed that  $\alpha'$  martensite is transformed into  $\alpha$  as a fine precipitate that is nucleated heterogeneously at martensite plate boundaries or at internal structures such as twins [19]. Many micro-twins have been observed inside  $\alpha$  phase as shown in Fig. 3d, which suggests the above-mentioned transformation of  $\alpha'$  to  $\alpha$ . It was reported that  $\alpha'$  would be unable to fully decompose into  $\alpha/\beta$  phases when the isothermal annealing temperature was below 650 °C [19]. Thermal mass ( $C_{th}$ ) is equivalent to heat capacity in a unit of J K<sup>-1</sup> that denotes the ability of an object to store thermal energy. For an object with a uniform composition,  $C_{th}$  can be approximately given by  $C_{th}=mc_p$ , where  $m$  is the mass of the object and  $c_p$  is the specific heat capacity of the material at constant pressure [20]. Therefore, the thicker sample will have a higher thermal mass, which means that it would experience a slower cooling rate. Furthermore, the thicker sample will be subject to a longer term annealing at a higher temperature in comparison with the thinner one. As we know, the temperature beneath the start plate was indicated as ~600-650 °C during EBM process. Since electron beam is the only heat source by constantly scanning over the powder bed and the heat was mainly transferred from top to bottom through the built parts, the temperature of the newly deposited layers for the thick samples (e.g. 5mm, 10mm and 20mm samples) must be higher than 650 °C that is sufficient to enable  $\alpha'$  decomposition. By contrast, the 1mm sample has a low thermal mass. Moreover, as mentioned above, it was built by the contour melting with a much faster beam scanning speed compared to that of in-fill hatch melting. Therefore, the temperature of the newly built layers of 1mm sample would be rapidly cooled down below 650 °C so that only a partial decomposition of  $\alpha'$  occurred. Thus, some retained  $\alpha'$  martensite could be observed in 1mm sample while a full  $\alpha/\beta$  microstructure was derived in the 10mm sample.

In order to further verify the above-mentioned martensitic formation and decomposition, FEM simulations were conducted in terms of the two models proposed in section 3. For the first model, scanning speeds of 4.5 m/s and 140 m/s were adopted to simulate the in-fill hatch melting and contour melting, respectively. The beam absorptivity was tuned so as to achieve a surface temperature of ~2400 °C, in accordance to the experimental measurements from Ref. [14]. Fig. 6a and b show that the thermal history for the two cases is very similar. This is due to the fact that, once the Ti-6Al-4V powder was melt, its cooling is mostly governed by the latent heat of fusion, which is obviously the same for both cases. However, the different scan speed affects the length of melt pool, where the contour melt has a longer melt pool compared to the in-fill hatch melt. It is found that there is a window of post-scan times where

the material is solid and the conditions are compatible with the formation of martensite (see Fig. 6a and b). In particular, a temperature below the martensite start temperature (800 °C [3]) and a cooling rate higher than 410 °C/s [18] occurred, which can be seen from the intersection points between the red and dashed blue lines, and between the green and dashed purple lines, in Fig. 6a and b. At the outside of the region in between the intersection points, either the temperature is above  $M_s$ , or the cooling rate is insufficient for martensitic formation.

The second model was used to investigate the decomposition of martensite. Temperature was extracted at three positions, namely, the top, the middle, and the bottom of the EBM builds. Results are compiled in Fig. 7. Starting from the “top” position (Fig. 7a), the temperature profiles clearly show that the temperature inside the 20mm, 10mm, 5mm and 1mm samples progressively decreases in this order. This effect is due to two reasons. Firstly, the higher thermal capacity of the thicker samples allow them to retain more heat compared to the thinner samples, because they have a larger mass. Moreover, thicker samples also have less time to cool down between successive scans, because the time required to scan thinner samples is shorter. This trend is also visible by comparing the temperature in the middle of the samples (Fig. 7b), where again the thicker samples have a higher average temperature than the thinner ones. However, a different temperature behavior is found at the lower part of the samples (Fig. 7c). This was due to the competitive effect of the different cooling time for each sample. In particular, the 20mm sample had the shortest time to cool down. Since the lower part of the sample is the most far from the heat source, heat simply did not have sufficient time to reach the bottom before the cooling time was over. Overall, Fig. 7 shows that the average temperature is higher for thicker samples. This means that the kinetics of martensite decomposition [19] into  $\alpha$  and  $\beta$  is expected to be higher for thicker samples. On the other hand, the 1mm sample showed a relatively low temperature, indicating a fast dissipation of heat into the powder. Therefore, the kinetics of martensitic decomposition is expected to be slow. This is the reason why some amounts of martensite are still retained inside the 1mm sample.

Fig. 8 exhibits an obvious increase in  $\beta$  phase spacing with the thickness in the four experimental samples. This suggests that a lower cooling rate was involved in the thicker samples as compared to the thinner samples, owing to the higher thermal mass. It also can be known from Fig. 6. Table 2 lists the  $\beta$  phase spacing as well as the corresponding Vickers microhardness of the four samples. The microhardness was decreased with the increase of  $\beta$  phase spacing. It can be explained by the classical Hall-Petch relation [21][22], *i.e.* the finer of the microstructure, the higher yield strength of the materials. It is found that the  $\alpha/\beta$  interface strengthening would play the primary role in determining the strength of EBM-built Ti-6Al-4V having a multiscale microstructure with cellular colony and basket-weave morphology [23]. Of particular note is that the highest microhardness obtained in 1mm sample was not

only due to its finest  $\beta$  phase spacing but also the retained  $\alpha'$  martensite. As an extremely high cooling rate was involved in EBM process, very fine  $\beta$  spacings were observed in this work. As a result, EBM-built Ti-6Al-4V will exhibit a high strength with the ultrafine microstructure. Moreover, the duplex microstructure, *i.e.* the soft rod-like  $\beta$  phase homogeneously embedded in the continuous hard  $\alpha$  phase, could provide a good ductility. As we know,  $\alpha'$  martensite is very hard, which allows a high strength but a low ductility of materials. It was previously accepted that martensite is supposed to be avoided in EBM-built Ti-6Al-4V via an elevated build temperature. However, it has been pointed out that the Ti-6Al-4V microstructure containing a mixture of  $\alpha$  and  $\alpha'$  will have superior mechanical properties [24]. If the control over microstructure can be achieved for EBM-built Ti-6Al-4V, *e.g.* obtaining a mixed microstructure of  $\alpha/\beta$  and  $\alpha'$ , it is promising to further improve its mechanical properties. From this work, big differences on microstructure and hardness can be seen for the EBM-built Ti-6Al-4V parts with different thicknesses. Thus, it is still challenging to build a complex part having a consistent microstructure via EBM.

## 5. Conclusions

In summary, four Ti-6Al-4V parts with different thicknesses were built using EBM in order to investigate its build thickness-dependent microstructure. A mixed microstructure of alternate  $\alpha/\beta$  with acicular  $\alpha'$  martensite was observed inside the 1mm sample, while only fully decomposed alternate  $\alpha/\beta$  microstructure occurred inside the 5mm, 10mm and 20mm samples. In addition, numerous micro-twins occurred inside both  $\alpha$  and  $\alpha'$  phases. It was found that  $\beta$  phase spacing constantly increases with the build thickness, meanwhile the microhardness was decreased accordingly. FEM simulations were designed to reproduce both the in-fill hatching and the contour melting scans, so as to investigate martensitic formation and decomposition. It was found that the temperature profiles and cooling rates are favorable for the formation of martensite. Moreover, simulations of the temperature profiles inside the samples showed that thicker samples had an average higher temperature compared to thinner samples, thus suggesting a faster kinetics for martensite decomposition for thick samples. This, in turn, was showed to depend on the combined effect of longer scan time, higher thermal mass, and shorter cooling times for the thicker samples compared to the thinner samples. The joint experiments and modeling provided detailed insights into the formation and decomposition of martensite as a function of sample thickness, thus suggesting a route towards the control of microstructure and mechanical properties in EBM-built Ti-6Al-4V.

## Acknowledgements

The authors are grateful for financial support provided by A\*STAR industrial additive manufacturing program: work package 3 (grant no. 132 550 4103) and the fruitful discussion with Dr. Nai Mui Ling

Sharon, Dr. Wang Pan and Dr. Raghavan Srinivasan. The authors acknowledge the use of resources in NTU Additive Manufacturing Centre supported by Singapore Economic Development Board (EDB).

## References

- [1] Chua CK, Leong KF. 3D Printing and Additive Manufacturing: Principles and Applications. 4th ed. Singapore: World Scientific; 2014.
- [2] Gibson I, Rosen DW, Stucker B. Additive Manufacturing Technologies. Boston: Springer US; 2010.
- [3] Boyer R, Welsch G, Collings EW. Materials Properties Handbook: Titanium Alloys. Materials Park (OH): ASM International; 1994.
- [4] Kok YH, Tan XP, Tor SB, Chua CK, Fabrication and microstructural characterisation of additive manufactured Ti-6Al-4V parts by electron beam melting, *Virtual Phys Prototyp* 2015; 10: 13-21.
- [5] Al-Bermani SS, Blackmore ML, Zhang W, Todd I. The Origin of Microstructural Diversity, Texture, and Mechanical Properties in Electron Beam Melted Ti-6Al-4V. *Metall Mater Trans A* 2010; 41: 3422-34.
- [6] Safdar A, Wei L-Y, Snis A, Lai Z. Evaluation of microstructural development in electron beam melted Ti-6Al-4V. *Mater Charact* 2012; 65: 8-15.
- [7] Gong X, Anderson T, Chou K. Review on powder-based electron beam additive manufacturing technology. *Manuf Rev* 2014; 1: 1-12.
- [8] Murr LE, Esquivel EV, Quinones SA, Gaytan SM, Lopez MI, Martinez EY, Medina F, Hernandez DH, Martinez E, Martinez JL, Stafford SW, Brown DK, Hoppe T, Meyers W, Lindhe U, Wicker RB. Microstructures and mechanical properties of electron beam-rapid manufactured Ti-6Al-4V biomedical prototypes compared to wrought Ti-6Al-4V. *Mater Charact* 2009; 60: 96-105.
- [9] Rafi HK, Karthik NV, Starr TL, Stucker BE, Mechanical property evaluation of Ti-6Al-4V parts made using Electron Beam Melting, *Proceedings of the Solid Freeform Fabrication Symposium* 2012; 526-535.
- [10] Xu W, Brandt M, Sun S, Elambasseril J, Liu Q, Latham K, Xia K, Qian M, Additive manufacturing of strong and ductile Ti-6Al-4V by selective laser melting via in situ martensite decomposition. *Acta Mater* 2015; 85: 74-84.
- [11] Rafi HK, Karthik NV, Gong HJ, Starr TL, Stucker BE, Microstructures and Mechanical Properties of Ti6Al4V Parts Fabricated by Selective Laser Melting and Electron Beam Melting. *JMEPEG* 2013; 22:3872-3883.
- [12] Zäh MF, Lutzmann S, Modelling and simulation of electron beam melting, *Prod Eng* 2010; 4: 15-23.

- [13] Jamshidinia M, Kong F, Kovacevic R, Numerical Modeling of Heat Distribution in the Electron Beam Melting of Ti-6Al-4V, *J Manuf Sci Eng* 2013; 135: 061010-1-14.
- [14] Yadroitsev I, Krakhmalev P, Yadroitsava I, Selective laser melting of Ti6Al4V alloy for biomedical applications: Temperature monitoring and microstructural evolution, *J Alloys Compd* 2014; 583: 404-409.
- [15] Vastola G, Zhang G, Pei QX, Zhang YW, Modeling and control of remelting in high-energy beam additive manufacturing, *Additive Manufacturing*, DOI 10.1016/j.addma.2014.12.004.
- [16] Neira A. Thermal modeling and simulation of Electron Beam Melting for rapid prototyping on Ti6Al4V alloys. PhD Thesis, North Carolina State University, Raleigh, NC, 2012
- [17] Zeng L, Bieler TR. Effects of working, heat treatment, and aging on microstructural evolution and crystallographic texture of  $\alpha$ ,  $\alpha'$ ,  $\alpha''$  and  $\beta$  phases in Ti-6Al-4V wire. *Mater Sci Eng A* 2005; 392: 403-14.
- [18] Ahmed T, Rack HJ. Phase transformations during cooling in  $\alpha+\beta$  titanium alloys. *Mater Sci Eng A* 1998; 243: 206-11.
- [19] Mur FG, Rodriguez D, J Planell. Influence of tempering temperature and time on the  $\alpha'$ -Ti-6Al-4V martensite. *J Alloys Compd* 1996; 234: 287-89.
- [20] Devoe H, Thermodynamics and chemistry. 2nd ed. College Park (Maryland): University of Maryland; 2014.
- [21] Armstrong RW. Engineering science aspects of the Hall-Petch relation. *Acta Mech* 2014; 225: 1013-28.
- [22] Lee D, Lee S, Lee C, Hur S. Effects of microstructural factors on quasi-static and dynamic deformation behaviors of Ti-6Al-4V alloys with widmanstätten structures. *Metall Mater Trans A* 2003; 34: 2541-8.
- [23] Tan XP, Kok YH, Tan YJ, Tor SB, Leong KF, Chua CK. On the graded microstructure and mechanical properties of additive manufactured Ti-6Al-4V by electron beam melting. submitted to *Acta Mater*.
- [24] Matsumoto H, Yoneda H, Sato K, Kurosu S, Maire E, Fabregue D, Konno TJ, Chiba A. Room-temperature ductility of Ti-6Al-4V alloy with  $\alpha'$  martensite microstructure. *Mater Sci Eng A* 2011; 528: 1512-20.

### Tables

Table 1. List of parameters used in the large-scale effective model.

Sample	Effective scanning speed (mm/sec)	Scanning time (sec)	Inter-layer cooling time (sec)
1mm	140000	0.0015	50.0
5mm	14	7.1	42.9
10mm	7	14.3	35.7
20mm	3.5	28.6	21.4

Table 2. The  $\beta$  phase spacing and Vickers hardness of the four experimental samples.

Sample	$\beta$ spacing ( $\mu\text{m}$ )	Vickers Hardness (HV)
1mm	0.283 $\pm$ 0.068	362.2 $\pm$ 6.0
5mm	0.463 $\pm$ 0.097	332.5 $\pm$ 4.6
10mm	0.610 $\pm$ 0.105	322.2 $\pm$ 5.4
20mm	0.813 $\pm$ 0.185	320.0 $\pm$ 4.9

## Figures

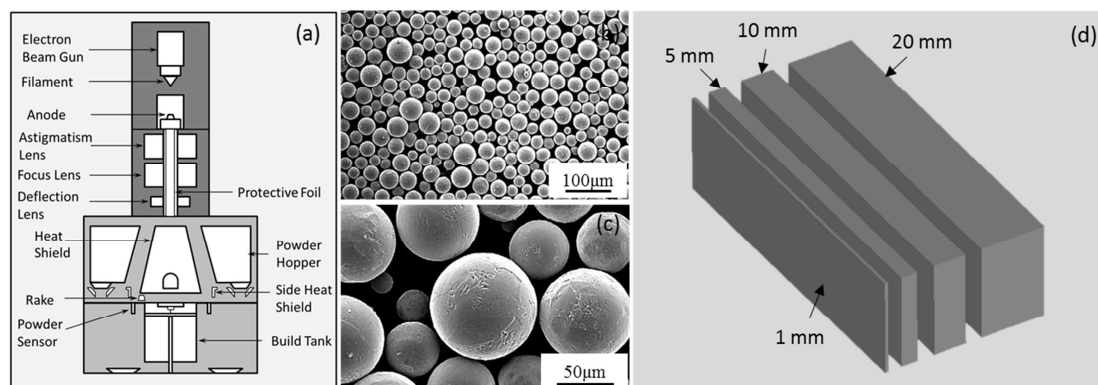


Fig. 1. (a) Schematic view of an EBM system. (b) and (c) SEM images showing the size distribution and morphology of Ti-6Al-4V ELI powder. (d) Schematic illustration of the four EBM-built samples with thicknesses of 1, 5, 10 and 20 mm.

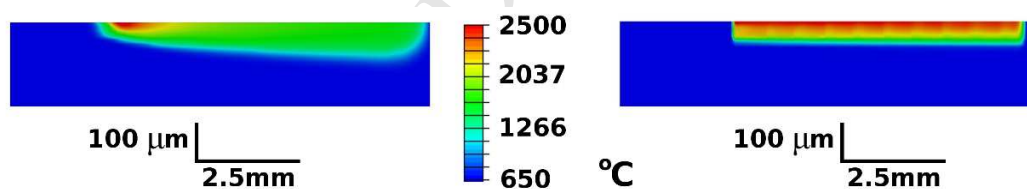


Fig. 2. (a) and (b) Temperature distribution obtained from the in-fill hatch melting and contour melting scan parameters, respectively. The length and height of each panel is 2.5 mm  $\times$  100  $\mu$ m, as shown in the schematics below each panel.

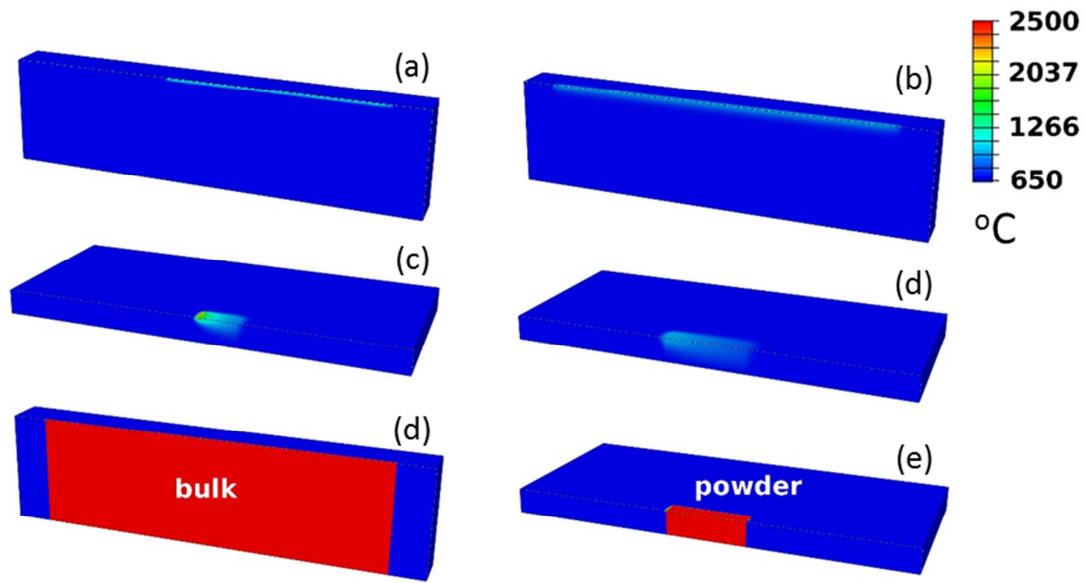


Fig. 3. Temperature distribution for the full-scale 1mm ((a) and (b)) and 20mm ((c) and (d)) samples with an effective beam heat source. (a) and (c) show the temperature during scanning, while (b) and (d) show the temperature during the cooling process. The samples are embedded into powder material, where the two phases are shown explicitly in (e) and (f) for the 1mm and the 20mm samples, respectively.

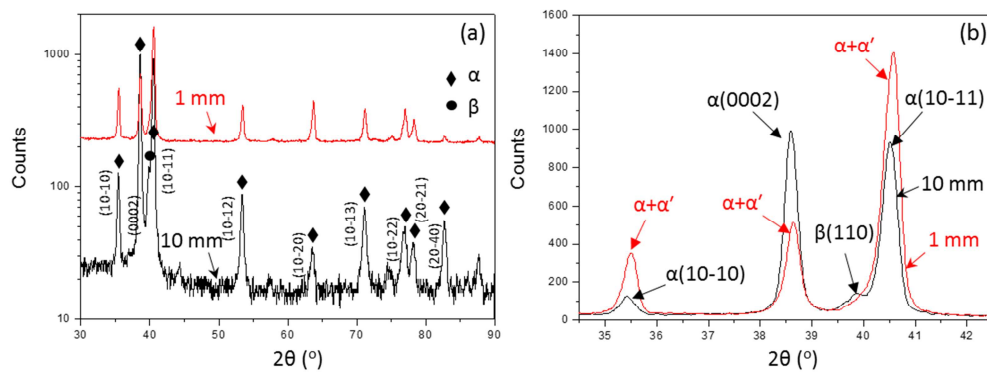


Fig. 4. (a) XRD profiles of 1mm (in red) and 10mm (in black) samples. (b) Locally enlarged XRD profiles in (a) showing the difference on the major peaks.



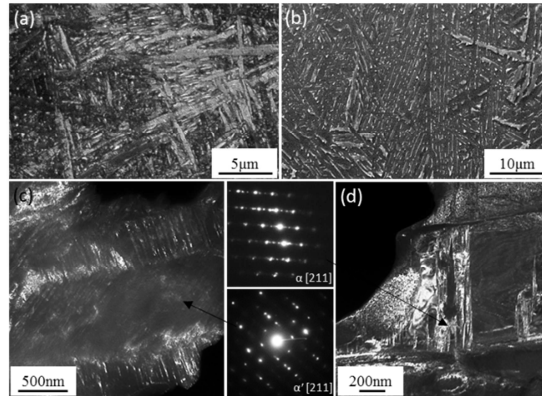


Fig. 5. SEM images showing (a) a mixed microstructure of alternate  $\alpha/\beta$  and  $\alpha'$  martensite in 1mm sample and (b) full microstructure of alternate  $\alpha/\beta$  in 5mm sample. Dark field TEM images showing (c)  $\alpha'$  martensite microstructure with numerous microtwins and (d) alternate  $\alpha/\beta$  microstructure with some microtwins.

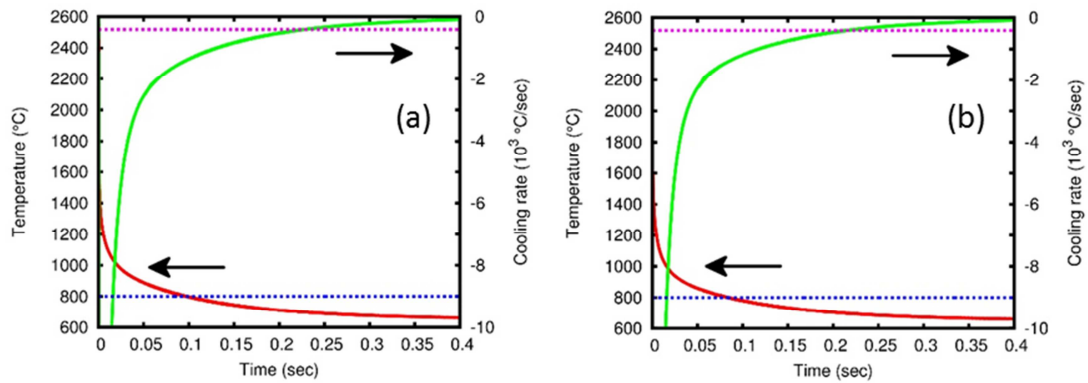


Fig. 6. (a) and (b) Temperature curves for a point right below the top surface for the case of Fig. 2. The temperature (red line, left scale) and cooling rate (green line, right scale) are shown for the in-fill hatch melting and contour melting, respectively. The dashed blue line is the martensite start temperature of 800 °C, and the dashed purple line is the critical cooling rate of 410 °C/s for martensitic formation.

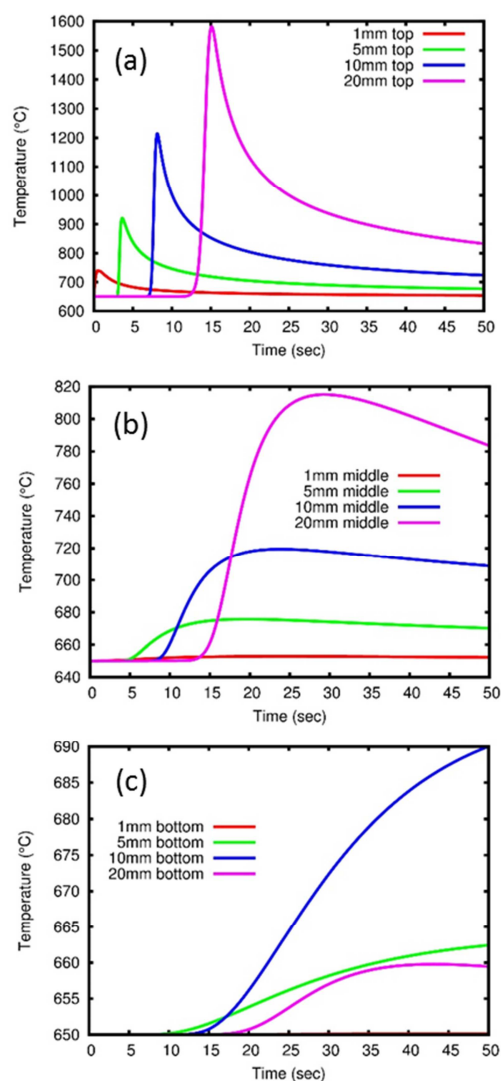


Fig. 7. Temperature evolution curves with respect to time for the positions of top (a), middle (b), and bottom (c) of the samples, respectively.

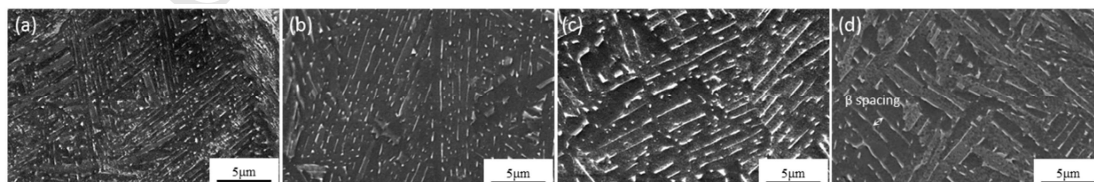


Fig. 8. SEM images showing the alternate  $\alpha/\beta$  microstructure of (a) 1mm, (b) 5mm, (c) 10mm and (d) 20 mm samples. Here  $\beta$  spacing is defined as the distance between two  $\beta$  rods (in white), as illustrated in (d) as an example.

### Highlights

Build geometry dependent microstructure and microhardness for EBM-built Ti-6Al-4V

Phase evolution involved in EBM process

FEM simulation of EBM process

$\alpha'$  martensite formation and its identification